Am J Transl Res 2023;15(11):6404-6412
www.ajtr.org /ISSN:1943-8141/AJTR0153683

Original Article

Design of electromagnetic tracking system for puncture needle of an intelligent puncture robot

Linlaisheng Luo[1], Xudong Guo[1], Bo Cheng[2], Zhaodong Zhang[2], Donglan Jiang[1]

[1]*School of Health Science and Engineering, University of Shanghai for Science and Technology, Shanghai, China;* [2]*Pound Kece (Shanghai) Intelligent Medical Technology Co., Ltd., Shanghai, China*

Received September 27, 2023; Accepted November 13, 2023; Epub November 15, 2023; Published November 30, 2023

Abstract: Objectives: The puncture needle of an intelligent puncture robot must accurately reach the target location early in the diagnosis of benign and malignant nodules and in the puncture ablation of malignant tumors. To track the position and the orientation of the puncture needle tip, an electromagnetic tracking system based on adaptive adjustment of excitation intensity and lock-in amplification is proposed. Methods: The system includes a time-sharing excitation device with multiple magnetic sources, a magnetic sensor, a signal processing device based on dual-phase lock-in amplifiers and a computing platform in the upper computer. With adaptive adjustment of excitation intensity, the time-sharing excitation device uses a microcontroller to control a direct digital synthesizer. Based on feedback from the magnetic sensor, the microcontroller time-shares the power amplifier to generate the required excitation current. Dual-phase lock-in amplifiers demodulate the magnetic sensor output after preamplification and filtering. Through analog-to-digital conversion and the serial interface, the digital signal is sent to the computing platform for solving by neighborhood particle swarm optimization algorithm, and the position and orientation of the puncture needle fixed with the magnetic sensor are obtained. Results: The experimental results within a 300 mm×300 mm×300 mm space show average position errors of 0.4467 cm (X-axis), 0.4154 cm (Y-axis), and 0.3766 cm (Z-axis). The overall average position error is 0.4129 cm, with a root mean square error of 0.4970 cm. Conclusions: The proposed electromagnetic tracking system can track the needle position and orientation of puncture robots in real-time, thereby enhancing puncture success rates and reducing puncture times.

Keywords: Puncture robot, electromagnetic tracking system, lock-in amplifier with dual-phase, adaptive adjustment of excitation intensity

Introduction

With the development of medical imaging technology, the detection rate of nodules is increasing in routine physical examination. In order to further determine the nature of the lesion, a biopsy of the patient is required. Needle biopsy, as a minimally invasive examination, is commonly used to identify malignancy [1]. Most mid- to late-stage cancer patients are not suitable for surgical resection. As a minimally invasive and accurate treatment method, the image-guided puncture ablation has become a research hotspot in the treatment of malignant tumors.

Manual puncture surgery guided by traditional medical images has problems such as clinical experience dependence, insufficient accuracy, increased operational damage and radiation, and operational fatigue [2]. The mortality rate of traditional Computed Tomography (CT)-guided percutaneous lung biopsy is 0.02% to 0.15%. Complications such as pneumothorax and hemorrhage often occur [3]. Dynamic ultrasound is of limited value for guidance of paracentesis procedures. Research by Qingyu Wang et al. found that during puncture and catheterization of the subclavian vein under dynamic ultrasound, real-time ultrasound cannot always clarify whether the actual operated blood vessel is the subclavian vein or the axillary vein [4].

In recent years, medical robots have attracted much attention, and puncture robots are a focal point in the field of medical robotics. Research by Wei Yuan et al. shows that compared to patients undergoing percutanouskyphoplasty

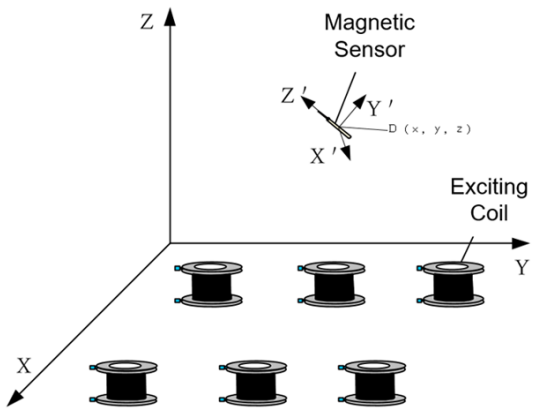

Figure 1. Diagram of electromagnetic tracking method.

treatment without robot assistance, the probability of complications is smaller when robot assistance is used [5]. The puncture surgery based on the puncture robot needs to establish a three-dimensional model of the organ to puncture and design the puncture path. Compared to manual puncture, the puncture robot can reach the lesion more accurately. However, the position of the soft organ (such as liver, lung, etc.) is not fixed. The liver moves with the breathing of the lungs, and the maximum movement range reaches 16.5±5.7 mm [6]. A commonly used clinical solution is to perform multiple CT verifications during surgery. However, a radiation dose of multiple CT scans during surgery has adverse effects on the health of patients and doctors [7]. Therefore, a current focus is to study the high-precision and real-time tracking system applied to the puncture robot.

There are many kinds of tracking technologies, including electromagnetic, optical, radio frequency, mechanical, and inertial tracking systems [8]. Kurita T developed vision-based high-precision position and orientation measurement systems with positional accuracy of approximately 3 μm and orientation accuracy of approximately 0.02 degrees [9]. Optical tracking technologies have a limited range and cannot work in the presence of obscure objects. Yanzhu Huang proposed an improved LANDMARC algorithm to improve the positioning accuracy of the algorithm due to the attenuation of indoor positioning signals by walls [10]. Radio frequency tracking technology has a large positioning range, but the positioning accuracy is not high. The force sensing system of the light manipulator developed by Shi Y has an average error of 7.6% in estimating the size and position of the impact force, and the average global-local repeated positioning error is 7.6%. Visual servo is 1.3 mm [11]. The accuracy of mechanical positioning is limited by the accuracy and stability of the mechanical structure. Duan Suchen used the inertial sensor to measure the human walking posture and used the Madgwick posture calculation algorithm. The position error was about 1% and the angle error was 3.4° [12]. Measurement errors of the inertial tracking system will accumulate over time, which causes poor anti-interference ability.

Electromagnetic tracking technology has the advantages of high precision, high reliability, and no line of sight [13]. Sadeghi Boroujeni P proposed a robust sliding mode controller. The proposed method can accurately and efficiently drive the capsule to follow the desired trajectory, with position and orientation accuracy of 0.53 mm and 0.69 degrees, respectively [14]. Zhao Jianhui et al. designed the electromagnetic field transmitting end of the matrix column of three orthogonal coil groups, and achieved a positioning frequency of 29 Hz [15]. In their paper, the electromagnetic tracking system was based on adaptive adjustment of excitation intensity and dual-phase lock-in amplification, which aims to improve the processing ability of weak signals and the tracking accuracy in the range of 300 mm×300 mm×300 mm.

Electromagnetic tracking principle and system design

The spatial Cartesian coordinate system XYZ is established. The excitation coil array of the tracking system is arranged on the XY plane. The magnetic sensor is fixed with the tip of the puncture needle of the puncture robot.

A space coordinate system X'Y'Z' in the magnetic sensor is established. The symmetric axis of the magnetic sensor is the Z' axis, as shown in **Figure 1**. Let six-dimensional variables (x, y, z, α, β, γ) represent the spatial position of the magnetic sensor, where (x, y, z) represents the position of the magnetic sensor and (α, β, γ) represents the Euler angles.

According to the Biot-Savart law, the magnetic flux density at (x, y, z) is:

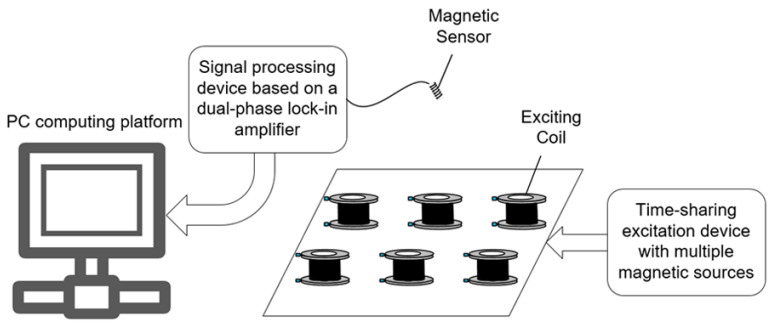

Figure 2. Overall design of the electromagnetic tracking system.

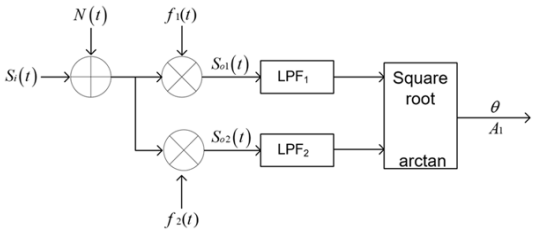

Figure 3. Schematic diagram of the dual-phase lock-in amplifier.

$$B(x,y,z)=\frac{N\mu_0}{4\pi}\iint_l\frac{Idl\times r}{r^3} \quad (1)$$

Where I is the root-mean-square value of the current of the excitation coil. dl is the micro-element on the excitation coil. μ_0 is the vacuum permeability. N is the turns of the excitation coils.

According to Taylor series expansion, the magnetic flux density B_x, B_y and B_z in the three axes of X, Y and Z can be obtained as:

$$\begin{bmatrix}B_z\\B_x\\B_y\end{bmatrix}=\frac{n\mu_0 Ia^2}{4(x^2+y^2+z^2)^{3/2}}\begin{bmatrix}\frac{3xz}{(x^2+y^2+z^2)^2+a^2}+\frac{105a^2(x^3z+xy^2z)}{8(x^2+y^2+z^2)^3}\\\frac{3yz}{(x^2+y^2+z^2)^2+a^2}+\frac{105a^2(x^3z+xy^2z)}{8(x^2+y^2+z^2)^3}\\2-\frac{3(x^2+y^2)}{(x^2+y^2+z^2)^2+a^2}+\frac{15a^2(x^2+y^2)}{2(x^2+y^2+z^2)^2}-\frac{105a^2(x^2+y^2)^2}{8(x^2+y^2+z^2)^3}\end{bmatrix} \quad (2)$$

Where a is the radius of the excitation coil.

The normal vector of the magnetic sensor along the coordinate axis X'Y'Z' can be decomposed as follows.

$$\begin{bmatrix}n_x\\n_y\\n_z\end{bmatrix}=\begin{bmatrix}\sin\alpha\cdot\cos\beta\\\sin\alpha\cdot\sin\beta\\\cos\alpha\end{bmatrix} \quad (3)$$

According to Faraday's law of electromagnetic induction, the magnitude of the induced electromotive force at the point (x, y, z) of the magnetic sensor with the number of turns n is:

$$e=-nS\left(n_x\frac{dB_x}{dt}+n_y\frac{dB_y}{dt}+n_z\frac{dB_z}{dt}\right) \quad (4)$$

By applying current with the same frequency to the 6 excitation coils in turns, 6 equations can be obtained. Thus, the orientation and attitude of the magnetic sensor can be solved.

As shown in **Figure 2**, the electromagnetic tracking system consists of a time-sharing excitation device with multiple magnetic sources, a magnetic sensor, a signal processing device based on a dual-phase lock-in amplifier, and a computing platform in the upper computer.

Among these, the time-sharing excitation device with multiple magnetic sources includes a direct digital synthesizer (DDS), a power amplification module, and an analog switch. A signal processing device based on a dual-phase lock-in amplifier is composed of a differential amplifier, a band-pass filter, and a dual-phase lock-in amplifier. The microcontroller controls the DDS to generate a sinusoidal signal. It drives the power amplifier to generate the required current according to the feedback of the magnetic sensor. The current passes through the excitation coil in time-sharing to generate an alternating magnetic field. The magnetic sensor converts the alternating magnetic field into an electrical signal. After pre-amplification and filtering, it is input to a dual-phase lock-in amplifier for amplitude and phase demodulation. Through analog-to-digital conversion and a serial interface, it is sent to the computing platform for solving.

Design of core circuits

Design of dual-phase lock-in amplifier

The structure of the dual-phase lock-in amplifier is shown in **Figure 3**, which mainly includes two multipliers and two low-pass filters.

$S_i(t)$ is the signal to be tested, which is defined as $S_i(t) = A_1\sin(\omega_1 t+\varphi_1)$. $N(t)$ is the total noise. $f_1(t)$ and $f_2(t)$ are two reference signals, which are defined as $f_1(t) = A_2\sin(\omega_1 t+\varphi_2)$, $f_2(t) = A_2\cos(\omega_1 t+\varphi_2)$, respectively. A_1 is the amplitude

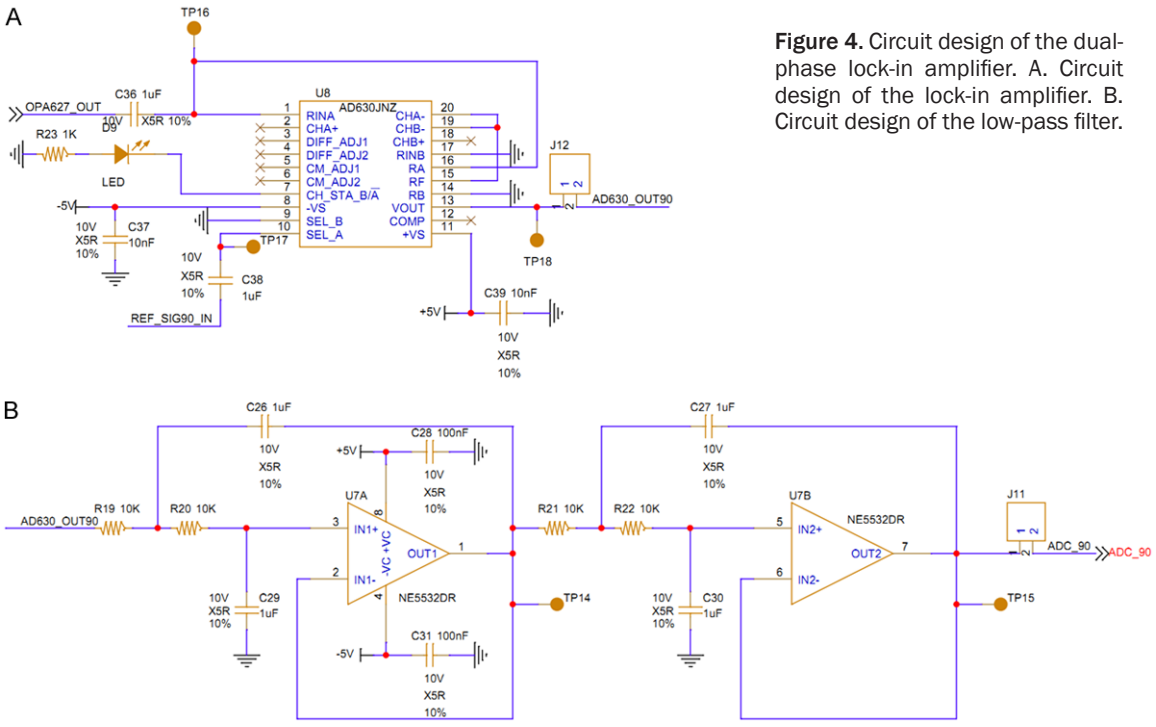

Figure 4. Circuit design of the dual-phase lock-in amplifier. A. Circuit design of the lock-in amplifier. B. Circuit design of the low-pass filter.

of the signal to be measured. A_2 is the amplitude of the reference signal. ω_1 is the angular frequency. The initial phase is φ_1 and φ_2. The phase difference between $f_1(t)$ and $f_2(t)$ is 90°.

After passing through the adder, the signal $S_i(t)$ to be tested and the total noise $N(t)$ are multiplied by the reference signal $f_1(t)$ and $f_2(t)$ respectively. The alternating current (AC) signal is filtered out after passing through the two low-pass filters LPF1 and LPF2. Thus the direct current (DC) signal is retained. VDC1 and VDC2 are obtained as:

$$V_{DC1} = \frac{A_1 A_2}{2}\cos(\varphi_1 - \varphi_2) \quad (5)$$

$$V_{DC2} = \frac{A_1 A_2}{2}\sin(\varphi_1 - \varphi_2) \quad (6)$$

Let $\theta = \varphi_1 - \varphi_2$. The sum of squares of formula (5) and formula (6) is:

$$V^2_{DC1} + V^2_{DC2} = \left[\frac{A_1 A_2}{2}\cos(\varphi_1 - \varphi_2)\right]^2 + \left[\frac{A_1 A_2}{2}\sin(\varphi_1 - \varphi_2)\right]^2 = \left(\frac{A_1 A_2}{2}\right)^2 \quad (7)$$

That is:

$$A_1 = \frac{2\sqrt{V^2_{DC1} + V^2_{DC2}}}{A_2} \quad (8)$$

When the signal to be tested and the reference signal are stable. V_{DC1}, V_{DC2} and A_2 are constants. The amplitude of the signal to be tested can be obtained by the inverse function as shown in formula (9).

$$\theta = \varphi_1 - \varphi_2 = \arctan\left(\frac{V_{DC2}}{V_{DC1}}\right) \quad (9)$$

Hence, the phase difference between the signal to be tested and the reference signal can be obtained by two DC components.

The system uses two pieces of AD630 and NE5532 to get a quadrature dual-phase lock-in amplifier. The circuit of the dual-phase lock-in amplifier is shown in **Figure 4**. In order to filter the DC bias of the signal to be measured and the reference signal, a 1 μF capacitor is connected in series at the input end. NE5532 is used to form a 4th-order Butterworth low-pass filter with a cutoff frequency of 15.9 Hz. A 100 nF capacitor is added to filter out the noise of the power supply.

Design of excitation circuit and reference signal generating circuit for demodulation

Electromagnetic tracking systems use DDS to generate excitation and demodulation reference signals. The DDS is a frequency synthesis method that directly samples and digitizes the reference clock. Then digital computing technology is used to generate the frequency [16].

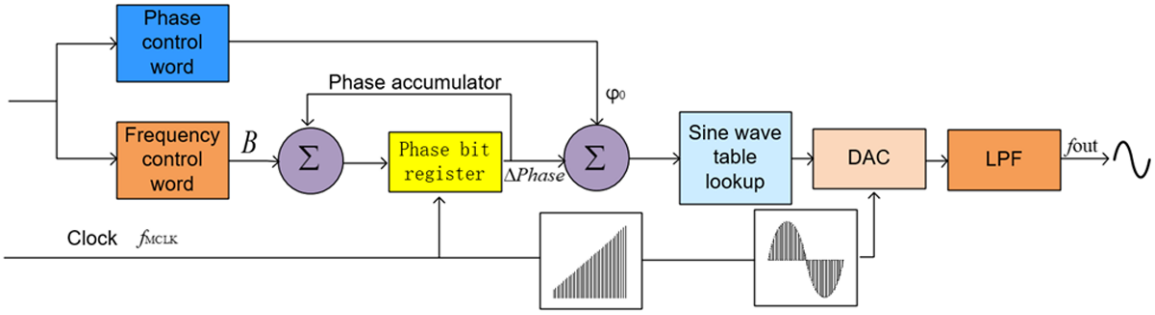

Figure 5. Signal generating principle of DDS.

Figure 5 is a schematic diagram of the DDS. f_{MCLK} is the system clock. $f$out is the frequency of the output signal. φ_0 is the initial phase. Every time the system clock is triggered, the accumulator adds the frequency control word B and the output $\Delta Phase$ of the phase register. The result is sent to the input terminal of the phase register. When the phase accumulator overflows, one clock cycle of $1/f$out is completed.

Based on the signal generating principle of DDS, S(t) can be obtained:

$$S_{(t)} = A \sin\left[2\pi\left(\frac{f_{MCLK} * B}{2^L}\right)t + \varphi_0\right] \quad (10)$$

Where L is the word length of the phase accumulator.

Based on the findings from (10), it is evident that when considering a DDS chip, any variation in the system clock and in the phase of the clock edge will result in a corresponding phase difference at the output of the DDS. From (5) and (6), it can be seen that only when (φ_1-φ_2) is stable, V_{DC1} and V_{DC2} keep a constant when the magnetic sensor is stationary. Thus, a stable phase difference must be maintained between the excitation signal and the reference signal.

In order to solve the output signal phase difference caused by DDS system clock error and clock edge phase difference, an excitation and demodulation reference signal generating circuit has been designed based on three DDS chips with shared oscillator and common reset pin. The generated frequency is 7.9 KHz. The excitation signal and the demodulation reference signal with an amplitude of 1 V and an initial phase of 0°, 0°, and 90° respectively. Both the signals with a phase of 0° and with a phase of 90° are selected as the reference signal. The signal with a phase of 0° is input to the power amplifier as an excitation signal. The two complementary outputs of the DDS chip are used to output a sinusoidal signal without DC bias.

Neighborhood particle swarm optimization algorithm with parameter self-tuning

The position and the attitude of the magnetic sensor can be calculated by the neighborhood particle swarm optimization algorithm with self-adjustment parameters. The implementation steps of the algorithm are as follows:

① Determine the individual number of the particle swarm. Initialize the particle swarm. Set the initial inertia weight ω, acceleration coefficients c_1 and c_2, the maximum iterations max, and the allowed error of the fitness value ε_1. The initial spatial position of the i-th particle is denoted by $x_i = (x_{i1},x_{i2},x_{i3},x_{i4},x_{i5},x_{i6})$. The initial velocity of the i-th particle is denoted by $v_i = (v_{i1},v_{i2},v_{i3},v_{i4},v_{i5},v_{i6})$.

② Substitute the position of each particle in the current generation into the fitness function. Update the best fitness value of each particle, the best position of each particle, the best fitness value of all the particles, and the best position of all the particles.

③ The best position of the $_i$-th particle is called the individual best position, recorded as $ps_i = (ps_{i1},ps_{i2},ps_{i3},...,ps_{iD})$. The position with the best fitness value experienced by all the particles in the population is called the global best position, which is recorded as $pg = (pg_1,pg_2,pg_3,...,pg_D)$. According to the individual best position, global best position, inertia

weight, and acceleration coefficient of the current generation, the velocity of the $_i$-th particle is obtained.

$$v_i = \omega v_i + c_1 r_1 (ps_i - x_i) + c_2 r_2 (pg - x_i) \quad (11)$$

Where r_1 and r_2 are two random numbers in the range [0, 1].

④ Determine whether the particle velocity of the new generation is out of bounds. If it is out of bounds, the particle velocity should be restricted. Then, the new velocity of each particle is substituted into the evolution equation to update the particle position. According to formula (12) and formula (13), the parameter value is adaptively adjusted.

$$\omega(t) = \omega_{\max} - \frac{t}{\max} \times (\omega_{\max} - \omega_{\min}) \quad (12)$$

$$c_2(t) = c_{\min} + \frac{t}{\max} \times (c_{\max} - c_{\min}) \quad (13)$$

Where ω is the inertia weight and c_2 is the acceleration weight. The subscript max refers to the maximum iterations. t is the current generation.

⑤ Judge whether the global best fitness value of the current generation is less than ε_1. Judge whether it reaches the allowed iterations *max*. If both conditions are not satisfied, jump to step ②. If the former condition is met and the latter condition is not met, the global best position of the particle will be saved as a seed and then will be removed from the population. A new particle will be randomly generated and added to the group. Jump to step ②. If the iteration is equal to *max*, the global best position of the particle swarm will be saved as a seed. Go to step ⑥.

⑥ The multiple seeds determined by particle swarm optimization are used as the initial point of Powell optimization algorithm. In Powell optimization, if the convergence criterion is met, the optimization is stopped. Among them, the optimization result with the minimum value of the objective function is the solution.

Experimental verification and result analysis

As shown in **Figure 6**, the experimental platform consists of a magnetic sensor, a time-sharing excitation device with multiple magnetic sources, a signal processing device based on dual-phase lock-in amplification, a Polhemus electromagnetic tracking system, and a six-degree-of-freedom pose adjustment device. The magnetic sensor is a multiple-layer solenoid coil constructed by us, that is cylindrical in shape with 0.6 mm diameter and 7 mm length. It consists of 1124 turns wound on a magnetic core. In the experiment, the six-degree-of-freedom pose adjustment device was used to fix the magnetic sensor. The position and attitude angle of the magnetic sensor were adjusted through the pose adjustment device. The Polhemus electromagnetic tracking system is used to measure the actual azimuth and attitude angle of the magnetic sensor in real time.

A total of 30 samples were tested in the experiment. First, the support rod is moved to Z=10 cm. while keeping the Z axis unchanged, the horizontal azimuth and attitude angle of the magnetic sensor are changed in turn to obtain 10 sets of data. Then the position and orientation of the magnetic sensor are calculated through the computing platform for each sample. The actual position and orientation of the sample is measured by the Polhemus electromagnetic tracking system. The above experimental process is repeated and the support rod is moved to Z=20 cm and Z=30 cm to obtain 10 sets of data respectively.

Figure 7 is a three-dimensional diagram of absolute error distribution. The absolute errors of the X, Y, and Z axes are all less than 0.6 cm, accounting for 56% of the total samples. It can be seen that the absolute errors of the samples are mainly distributed between 0-0.6 cm.

The maximum error, minimum error, average error, and root mean square error of the sample are shown in **Table 1**. The average error of X, Y, and Z axes is 0.4129 cm. The average root mean square error of X, Y, and Z axes is 0.4970 cm.

Figure 8 is a relative error distribution diagram. There are 23 samples with relative error range of [0, 5%) along X-axis, accounting for 76.7% of the total samples. There are 7 samples with relative error range of [5%, 15%) along X-axis, accounting for 23.3% of the total samples. There are no samples with relative error range of [15%, 100%] along X-axis. The relative error along the X axis is smaller than the other axes. There are 20 samples with the relative error

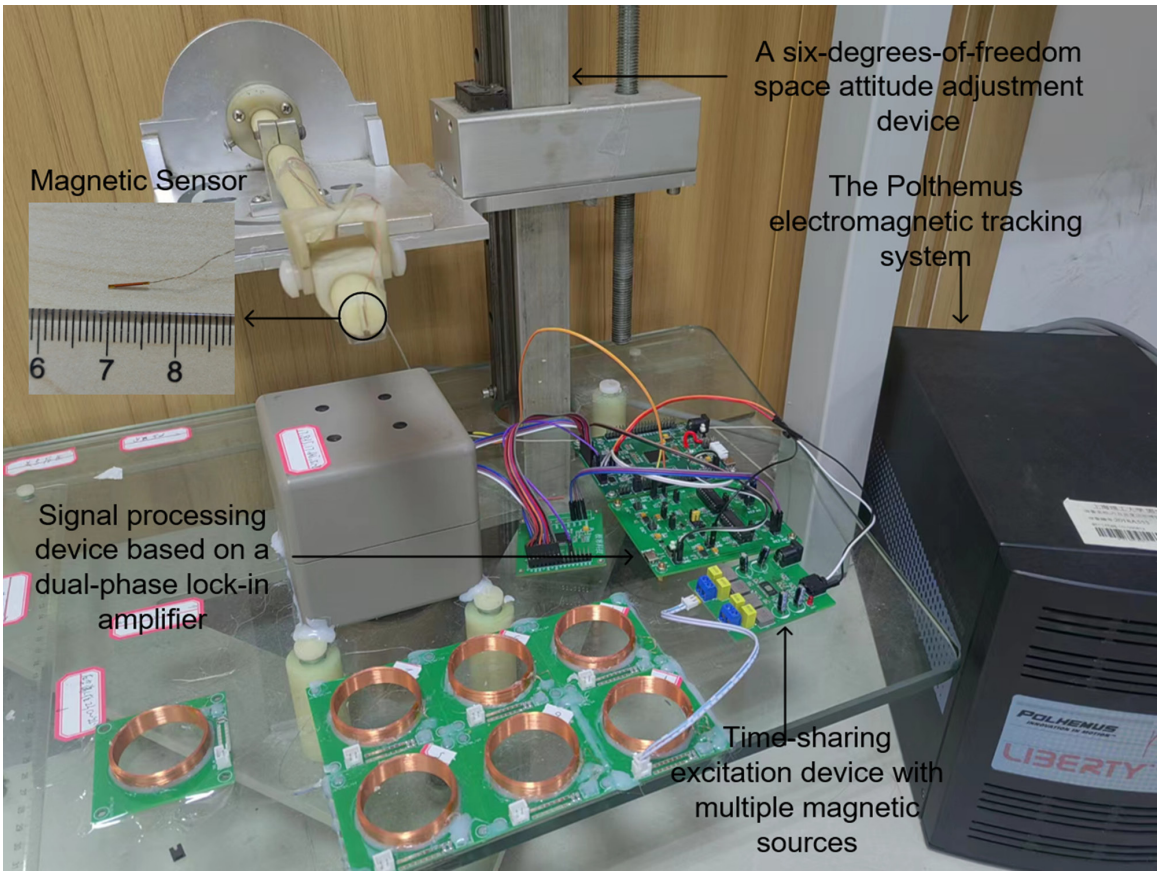

Figure 6. Experimental testing platform.

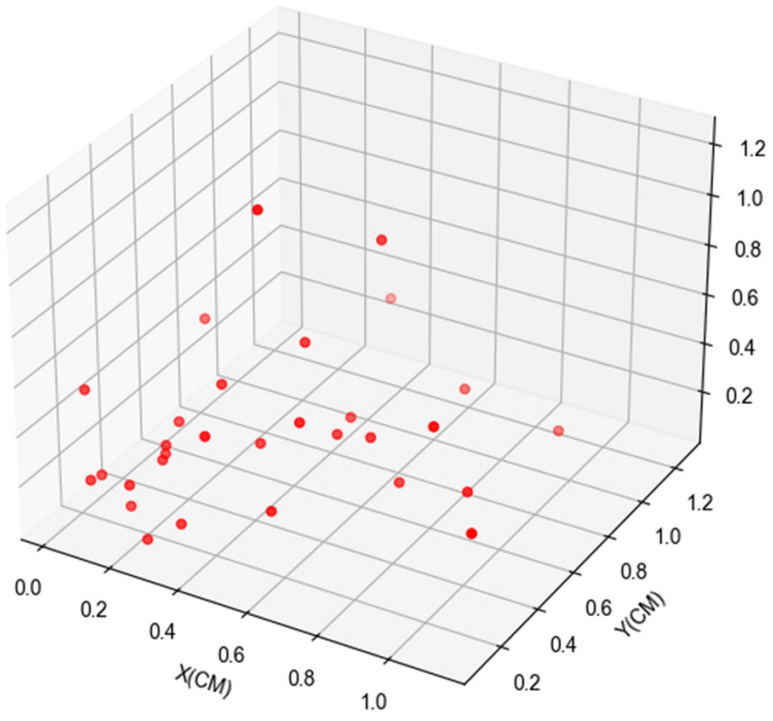

Figure 7. Absolute error distribution diagram.

range of [5%, 15%] along the Z-axis, accounting for 66.7% of the total samples. Only 1 sample is with the relative error range of [15%, 100%]. There are 5 samples with relative error range of [0, 5%] along the Y-axis, accounting for 16.7% of the total samples. There are 11 samples with relative error range of [5%, 15%] along the Y-axis, accounting for 36.7% of the total samples.

Conclusion

In this paper, starting from the principle of electromagnetic induction positioning, an electromagnetic tracking system based on adaptive adjustment of excitation intensity and lock-in amplifier

Table 1. Positional error of X, Y, and Z axes

Error Component	Maximum Error	Minimum Error	Average Error	Root Mean Square Error
E_x	1.1281 cm	0.0172 cm	0.4467 cm	0.5334 cm
E_y	1.2679 cm	0.0925 cm	0.4154 cm	0.5083 cm
E_z	1.2217 cm	0.0692 cm	0.3766 cm	0.4495 cm

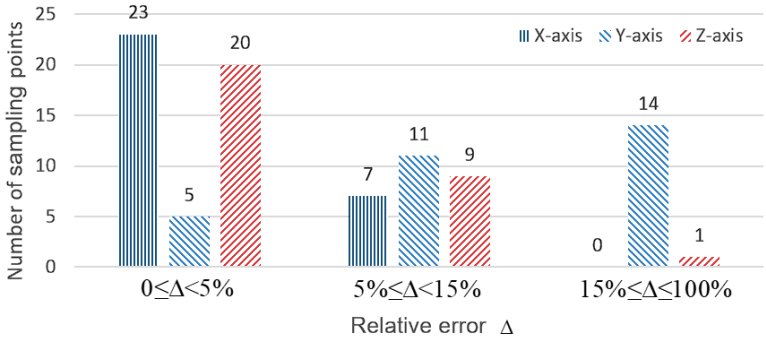

Figure 8. Bar graphs of the relative error.

with dual phases is designed. The electromagnetic tracking system is composed of a time-sharing excitation device with multiple magnetic sources, a magnetic sensor using a solenoid coil, a signal processing device based on a dual-phase lock-in amplifier and a computing platform. To solve the output signal phase difference caused by DDS system clock error and clock edge phase difference, an excitation circuit and a reference signal generating circuit for demodulation have been designed based on three DDS chips with shared oscillator and common reset pin. Through the neighborhood particle swarm optimization algorithm of global optimization, the position and orientation of the target are solved. The experimental results show that in the space of 300 mm×300 mm×300 mm the average position errors of the X-axis, Y-axis, and Z-axis are 0.4467 cm, 0.4154 cm, and 0.3766 cm respectively. The average position error is 0.4129 cm and the root mean square error is 0.4970 cm. Using a smaller magnetic sensor with 0.6 mm diameter, the electromagnetic tracking system has broader application, and it can be fixed in a narrow space suitable for smaller operation instruments.

To further improve localization precision, a global error correction technique should be investigated to correct the systematical errors. Within the operational space, a dataset can be established between the true location of the needle and the location tracked by the tracking system. Research needs to be conducted on an error correction algorithm based on the dataset.

Acknowledgements

This study is supported by National Natural Science Foundation of China (No. 623-73253); Shanghai Municipal Science and Technology Major Project (2021SHZDZX); Shanghai Science and Technology Innovation Action Plan (22S31902200); and Shanghai Interventional Medical Device Engineering Technology Research Center (18DZ2250900).

Disclosure of conflict of interest

None.

Address correspondence to: Xudong Guo, School of Health Science and Engineering, University of Shanghai for Science and Technology, Shanghai, China. E-mail: guoxd@usst.edu.cn

References

[1] Iguchi T, Hiraki T, Matsui Y, Tomita K, Uka M, Tanaka T, Munetomo K, Gobara H and Kanazawa S. CT-guided biopsy of lung nodules with pleural contact: comparison of two puncture routes. Diagn Interv Imaging 2021; 102: 539-544.

[2] Andria G, Attivissimo F, Di Nisio A, Lanzolla AML, Larizza P and Selicato S. Development and performance evaluation of an electromagnetic tracking system for surgery navigation. Measurement 2019; 148: 106916.

[3] He L, Meng Y, Zhong J, Tang L, Chui C and Zhang J. Preoperative path planning algorithm for lung puncture biopsy based on path constraint and multidimensional space distance optimization. Biomed Signal Process Control 2023; 80: 104304.

[4] Wang Q, Cai J, Lu Z, Zhao Q, Yang Y, Sun L, He Q and Xu S. Static ultrasound guidance VS. anatomical landmarks for subclavian vein puncture in the intensive care unit: a pilot randomized controlled study. J Emerg Med 2020; 59: 918-926.
[5] Yuan W, Cao W, Meng X, Zhu H, Liu X, Cui C, Tao L and Zhu Y. Learning curve of robot-assisted percutaneous kyphoplasty for osteoporotic vertebral compression fractures. World Neurosurg 2020; 138: e323-e329.
[6] Chen B, Weber N, Odille F, Large-Dessale C, Delmas A, Bonnemains L and Felblinger J. Design and validation of a novel MR-compatible sensor for respiratory motion modeling and correction. IEEE Trans Biomed Eng 2017; 64: 123-133.
[7] Ma Y, Yang Z, Wu W, Xie H and Gu L. Target localization during respiration motion based on LSTM: a pilot study on robotic puncture system. Int J Med Robot 2021; 17: e2247.
[8] Sorriento A, Porfido MB, Mazzoleni S, Calvosa G, Tenucci M, Ciuti G and Dario P. Optical and electromagnetic tracking systems for biomedical applications: a critical review on potentialities and limitations. IEEE Rev Biomed Eng 2020; 13: 212-232.
[9] Kurita T, Kasashima N and Matsumoto M. Development of a vision-based high precision position and orientation measurement system to facilitate automation of workpiece installation in machine tools. CIRP J Manuf Sci Technol 2022; 38: 509-517.
[10] Huang Y, Li L, Hu L, Huang H, Liao Z and Wang J. Application of improved LANDMARC indoor positioning algorithm in neurology medical care monitoring and positioning system. World Neurosurg 2020; 138: 680-687.
[11] Shi Y, Jin S, Zhao Y, Huo Y, Liu L and Cui Y. Lightweight force-sensing tomato picking robotic arm with a "global-local" visual servo. Comput Electron Agric 2023; 204: 107549.
[12] Jiang W and Tan X. Low cost inertial sensor attitude fixation algorithm and accuracy analysis. Adv Space Res 2023; 72: 2270-2282.
[13] Brastianos H, Janssen N, Akingbade A, Olding T, Vaughan T, Tamas U, Lasso A, Joshi C, Korzeniowski MA, Fichtinger G and Falkson CB. Pilot study of use of electromagnetic tracking technology to reconstruct catheter paths in breast brachytherapy. Int J Radiat Oncol Biol Phys 2020; 108: S186.
[14] Sadeghi Boroujeni P, Nejat Pishkenari H, Amiri Chimeh H, Moradi H and Vossoughi G. Five-degree-of-freedom robust control of a magnetic endoscopic capsule using an electromagnetic system. Control Engineering Practice 2023; 134: 105484.
[15] Zhao J, Zhong P, Yuan Z, Zhao W and Zhang T. A new electromagnetic positioning model with single coil receiver for virtual interventional surgery. Journal of System Simulation 2023; 35: 579-591.
[16] Rybin YK and Petlina TA. Basic metrological properties of electronic oscillators with direct digital synthesis. Measurement 2017; 98: 243-249.